Colloquia: GCM8

Influence of the hydrostatic and the deviatoric components of stress on ductility of metals

D. Corallo, G. La Rosa and G. Mirone

Dipartimento di Ingegneria Industriale e Meccanica, Università di Catania - Catania, Italy

Summary. — Failure of ductile metals occurring as microvoids growth is known to strongly depend on the stress triaxiality parameter which is a conventional measure of the first stress invariant normalized with respect to the equivalent von Mises stress, which in turn is a conventional measure of the second stress invariant. The triaxiality parameter is usually assumed to not influence the stress-strain behavior of metals according to the von Mises plasticity. The effects of the Lode angle and of the stress triaxiality are investigated here with regard to ductile failure and to the stress-strain behavior. Experimental results and numerical predictions are compared for different metals and different specimen geometries, by investigating about various failure criteria and a procedure for the post-necking stress-strain characterization. Tensile specimens and notched plates are loaded up to failure, then finite elements simulations are verified by comparison with experimental data. The verified numerical data are then used to calculate local variables within the volume of failing specimens; the knowledge of these local variables enables to predict global and local failure conditions according to the selected failure models.

PACS 62.20.mt – Cracks.
PACS 83.50.-v – Deformation and flow.
PACS 62.20.fk – Ductility; malleability.
PACS 62.20.fq – Plasticity and superplasticity.

1. – Functions and experiments for hardening determination

The elastoplastic characteristic of structural metals, in case of isotropic hardening, is given by a function relating the pressure-insensitive von Mises stress to the equivalent plastic strain $\sigma_{\mathrm{eq}}(\varepsilon_{\mathrm{eq}})$ [1-4]. Recent studies [5-9] postulated that a realistic evolution of the yield surface should include a small (sometimes negligible) dependence on the hydrostatic stress, and a more pronounced dependence on the third invariant of deviatoric stress. This idea is supported by experimental results and suggests that the yield surface is a tapered cylinder with a non-circular cross-section.

The two terms for characterizing the isotropic hardening are defined as in (1) and (2), respectively:

$$(1) \qquad \sigma_{\mathrm{eq}} = \sqrt{\frac{1}{2}\left[(\sigma_z - \sigma_r)^2 + (\sigma_z - \sigma_\vartheta)^2 + (\sigma_\vartheta - \sigma_r)^2\right]},$$

$$(2) \qquad \varepsilon_{\mathrm{eq}} = \sqrt{\frac{2}{3}\left[\varepsilon_z{}^2 + \varepsilon_r{}^2 + \varepsilon_\vartheta{}^2\right]},$$

z, r, θ, respectively, are the axial, radial and hoop directions in a cylindrical principal coordinates system, σ_i is the i-th principal stress and ε_i are the principal plastic strains. The relationship between σ_i and s_i is based on the definition of the hydrostatic stress σ_H:

$$(3) \qquad \sigma_H = \frac{\sigma_1 + \sigma_2 + \sigma_3}{3}, \qquad s_i = \sigma_i - \sigma_H.$$

The elastoplastic material curves are derived from tensile tests on round smooth specimens, by calculating the true stress and true strain defined as in eq. (4) which, in case of uniaxiality and uniformity of stress, coincide with σ_{eq} and $\varepsilon_{\mathrm{eq}}$:

$$(4) \qquad \sigma_{\mathrm{true}} = \frac{F}{\pi \cdot a^2} = \sigma_{z\mathrm{avg}} \quad \forall r,$$

uniformity and volume conservation allow to derive the true strain:

$$(5) \qquad \begin{array}{l} \varepsilon_{\mathrm{true}} = 2 \cdot \ln\frac{a_0}{a} = \varepsilon_{z\mathrm{avg}} = 2 \cdot \varepsilon_r = 2 \cdot \varepsilon_r; \\ \varepsilon_{\mathrm{eq}}(r) = \varepsilon_z(r) = 2 \cdot \ln\frac{a_0}{a}\,; \end{array}$$

a and a_0 being the current and the initial values for the radius of the minimum cross-section. So σ_{true} and $\varepsilon_{\mathrm{true}}$, conventionally named true stress and true strain, can be easily calculated from load-diameter measurements and coincide with σ_{eq} and $\varepsilon_{\mathrm{eq}}$ up to the necking initiation.

When the strain concentrates around the weakest cross-section of the specimen and necking takes place, the shape of the specimen becomes progressively hourglass-like and increasing nonuniformity and triaxiality of the stress state occurs, invalidating eqs. (4) and (5).

Figure 1 from [10] shows the stress distributions along the radial abscissa of the neck section for a 20MnMoNi55 steel ($\varepsilon_N = 0.1$), just after necking initiation ($\varepsilon_{\mathrm{true}} = 0.2$) and at incipient failure ($\varepsilon_{\mathrm{true}} = 1.1$). Estimations from FE analyses and from the MLR model are almost coincident and well underline how significant departure from uniaxiality may occur at large post-necking strains. The implicit FE analyses were performed with axisymmetric 8-noded elements under the hypotheses of large strains (updated Lagrangian formulation) and isotropic hardening, while the extended MLR method presented in [10] was based on approximate shapes for the distribution of hydrostatic stress along the neck radius.

This means that now σ_{true} and $\varepsilon_{\mathrm{true}}$ differ from the von Mises stress and the equivalent plastic strain respectively, so a method is required for calculating σ_{eq} and $\varepsilon_{\mathrm{eq}}$ from the post-necking experimental data [11-15].
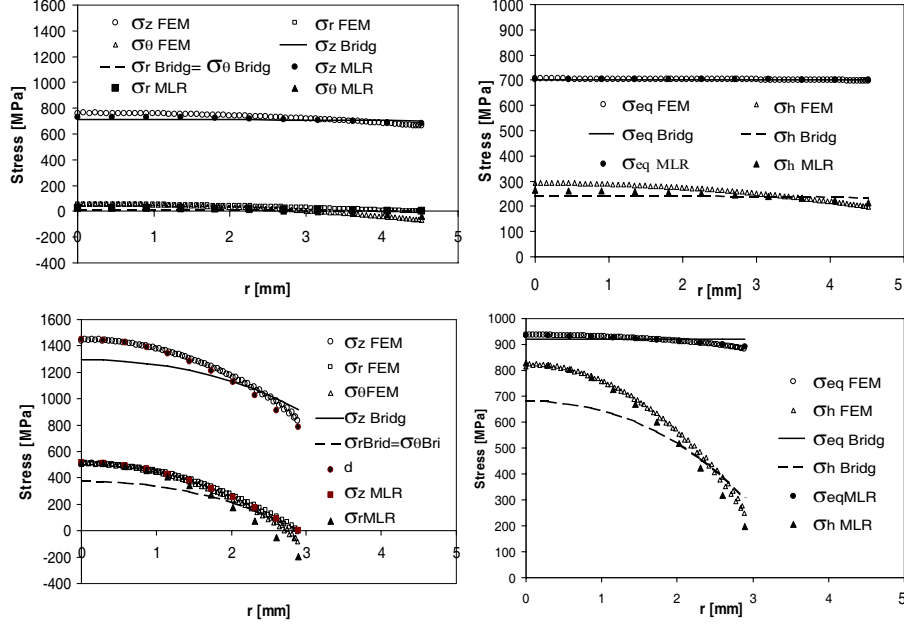
Fig. 1. – Stress distributions for a 20MnMoNi55 steel at different strain levels.

The MLR model presented in [16] is used in this paper for transforming the function $\sigma_{\text{true}}(\varepsilon_{\text{true}})$ into an estimation of $\sigma_{\text{eq}}(\varepsilon_{\text{eq}})$ by simply multiplying the true stress times a material-independent corrective function $MLR(\varepsilon_{\text{eq}} - \varepsilon_N)$. ε_N is a material-constant expressing the value of logarithmic strain at which the necking localization initiates and the maximum load is achieved; ε_N is typical of each metal and is also known as the Considére strain.

$$(6) \qquad \sigma_{\text{eq}}(\varepsilon_{\text{eq}}) = \sigma_{\text{true}}(\varepsilon_{\text{true}}) \cdot MLR(\varepsilon_{\text{eq}} - \varepsilon_N);$$

the corrective function MLR is expressed by the 4th-order polynomial of eq. (7):

$$(7) \quad MLR(\varepsilon_{\text{eq}} - \varepsilon_N) = 1 - 0.6058 \cdot (\varepsilon_{\text{eq}} - \varepsilon_N)^2 + 0.6317 \cdot (\varepsilon_{\text{eq}} - \varepsilon_N)^3 - 0.2107 \cdot (\varepsilon_{\text{eq}} - \varepsilon_N)^4.$$

This is an approximate function able to translate the experimental σ_{true} into an estimation of σ_{eq}, for many ductile steels, aluminium alloys or pure copper undergoing quasi-static deformations up to $3 \times 10^{-3}\,\text{s}^{-1}$.

It was found by best-fitting the results of various numerical analyses validated with as many experimental tests, and applies in the range of strains up to 100% above the necking strain ε_N.

The rationale of this correction method is that the necking is a geometry-driven form of instability, somehow similar to the buckling, so the material may influence when the necking initiates (through the strain ε_N) but, for a given set of shape and constraints (round smooth specimens in tension), this instability distorts the spatial distributions of stresses and strains in a material-independent way.

ROUND SPECIMENS (ALL METALS)
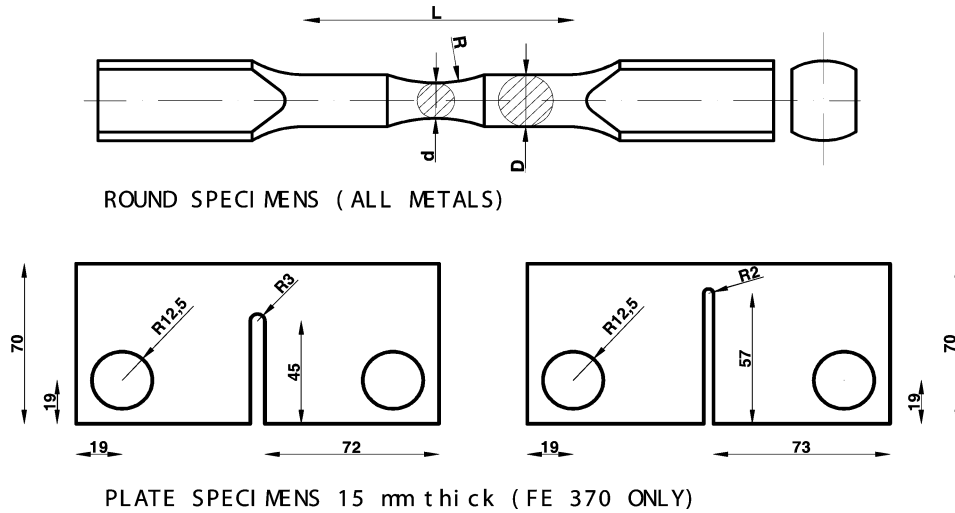
PLATE SPECIMENS 15 mm thick (FE 370 ONLY)

Fig. 2. – Round specimens geometry.

The necking strain is usually below 0.3 and the failure strain of smooth specimens made of ductile metals may lie beyond 1.5; then, a post-necking correction may be required over more than 80% of the material strain range.

In this work, various sets of specimens from different metals are analyzed according to table I and fig. 2.

Tensile tests are performed with an Instron 4920 test machine and with a Zwick Z100 test machine. Video sequences are acquired during the tests of smooth and notched round specimens, and the varying values of the current diameter of the minimum cross-section, $2a$, are successively measured by image analysis; then, the current cross-section radius a

TABLE I. – *Materials and specimens dimensions.*

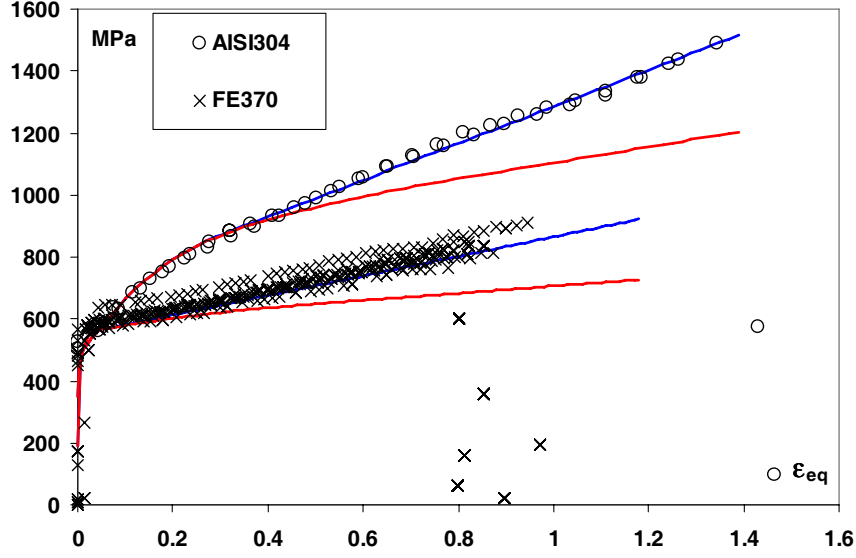| Metal	Short name	Specimen	d (mm)	D (mm)	R (mm)	L (mm)
Stainless-steel AISI 304	*AISI 304*	Smooth	9	9	- - -	55
		R30	6	9	30	55
		R15	6	9	15	55
		R5	6	9	5	55
		R2	6	9	2	55
		R20	6	9	20	50
		R10	6	9	10	50
ASTM A 284 - FE 370	*FE370*	Smooth	9	9	- - -	55
		R12	6	9	12	55
		R6	6	9	6	55
		R3	6	9	3	55
		PL-R3	-	-	-	-
		PL-R2	-	-	-	-

Fig. 3. – True stress-true strain from smooth specimens and MLR-derived $\sigma_{\mathrm{eq}}(\varepsilon_{\mathrm{eq}})$ curves.

from measurement and the current load F from the testing machine are used to calculate σ_{true} and $\varepsilon_{\mathrm{true}}$, according to eqs. (4) and (5).

For each metal, the experimental true stress-true strain data from smooth specimens is best-fit by polynomials; the resulting function is then used to calculate $\sigma_{\mathrm{eq}}(\varepsilon_{\mathrm{eq}})$ through the MLR correction according to eq. (6).

The resulting curves expressing either σ_{true} or σ_{eq} are shown in fig. 3 for the smooth specimens of all the metals tested.

The bifurcation between σ_{true} and σ_{eq} in fig. 3 evidences that necking initiates, while before its occurrence σ_{eq} is perfectly coincident with σ_{true}, as in eq. (4).

The triaxiality factor TF and the normalized Lode angle θ_N, both interacting with the yield surface and with ductile damage, are defined as follows:

$$(8) \qquad\qquad TF = \frac{\sigma_H}{\sigma_{\mathrm{eq}}},$$

$$(9) \qquad\qquad \theta_N = 1 - \frac{2}{\pi} \cdot \arccos\left[\frac{\frac{27}{2} \cdot s_1 \cdot s_2 \cdot s_3}{\sigma_{\mathrm{eq}}^{3}}\right],$$

where σ_i and s_i are principal stresses and the principal deviatoric stresses, respectively, expressed in a coordinate system 1-2-3.

The parameter TF ranges in $[-\infty, +\infty]$, its characteristic values are $1/3$ for uniaxial tensile stress $(\sigma, 0, 0)$ with $\sigma > 0$, 0 for pure shear $(\sigma, -\sigma, 0)$, and $-1/3$ for uniaxial compression $(\sigma, 0, 0)$ with $\sigma < 0$.

θ_N ranges in $[-1, 1]$ and is equal to 1 for stress states of the kind $(\sigma_A, \sigma_B, \sigma_B)$ with σ_A and $\sigma_B > 0$, 0 for principal stresses like $(\sigma_A, \sigma_B, (\sigma_A + \sigma_B)/2)$, and -1 for $(\sigma_A, \sigma_B, \sigma_B)$ with σ_A and $\sigma_B < 0$; the first of these three stress states is typical of the center of axisimmetric geometries loaded in tension and includes the uniaxial tension as a particular

case when $\sigma_B = 0$, the second is a generic plastic plane strain state and includes the pure shear as a special case with $\sigma_A = \sigma_B$, the third corresponds to axisimmetric compression and degenerates in uniaxial compression when $\sigma_B = 0$.

Then, TF and θ_N for smooth tensile round specimens may evolve in two different ways depending on the strain level and the material point considered: prior to necking, the uniformity and uniaxiality of the stress state makes $TF = 1/3$ and $\theta_N = 1$ wherever in the specimen, but, after necking initiates, the stress distributions become increasingly non-uniform inducing variability and non-uniformity also in the distributions of TF and θ_N. At the neck center ($r = 0$) TF may increase well beyond $1/3$ but the Lode angle does not deviate from unity during the entire load history, because here the pre-necking uniaxial tension and the post-necking axisimmetric tension induce the same value of θ_N. Instead, at the outer circumference of the neck section ($r = a$), the initial pre-necking uniaxial tension becomes a post-necking biaxial stress state, so that the post-necking evolution of TF and θ_N at this material point is completely different from the "axisimmetric" evolution the same variables experience on the neck center. The stress states at material points between the neck center and outer radius, $0 < r <$ a, are intermediate between those described.

Things change for round notched specimens because now the stress distributions are non-uniform already before necking initiation. So θ_N at the center of the minimum cross-section remains constant and equal to 1 due to axisymmetry, but the initial biaxiality at $r = a$ implies that θ_N evolves differently than it does for smooth specimens.

In the notch root area of the flat plates, the stress state may tend to plane strain on the half-thickness plane, so that θ_N may be close to zero, while TF has a great variability depending on the strain level and the position of material points along the thickness.

Distributions of θ_N, TF and other parameters of interest, calculated by FE for all the specimens tested, will be discussed in the next sections of the paper after the assessment of accuracy in numerical simulations.

2. – Damage modeling

The first series of failure predictions in this work is based on the Tresca model, by assuming that a material point fails when the maximum shear stress in a material point reaches a critical value.

$$(10) \qquad\qquad \tau_{\max}(\varepsilon_{\mathrm{eq}}) \leq \tau_{\max}(\varepsilon_f) = \tau_{\mathrm{cr}},$$

where τ_{cr} is a material constant and ε_f is the value of local $\varepsilon_{\mathrm{eq}}$ at failure.

Equation (10) clearly expresses a damage function [17-31] (so the Tresca model is indicated as a DF-based failure model), in fact, the damage function $\tau_{\max}(\varepsilon_{\mathrm{eq}})$ depends on how the structure is shaped constrained and loaded, and the Tresca model is not capable of directly giving failure strains without the knowledge of the stress-strain history.

The second model used here derives from a proposal by Bao and Wierzbicki [32,33], is indicated as the W1 model and assumes that, in the range of positive triaxialities above $1/3$, the failure strain can be expressed as in eq. (11):

$$(11) \qquad\qquad \varepsilon_f = \frac{D_{\mathrm{cr}}}{TF_{\mathrm{avg}}(\varepsilon_f)}$$

with D_{cr} being a material constant and TF_{avg} being the local stress triaxiality at a material point, averaged over the strain history up to the current $\varepsilon_{\mathrm{eq}}$:

$$(12) \qquad TF_{\mathrm{avg}}(\varepsilon_{\mathrm{eq}}) = \frac{1}{\varepsilon_{\mathrm{eq}}} \int_0^{\varepsilon_{\mathrm{eq}}} TF(\varepsilon_{\mathrm{eq}}) \cdot \mathrm{d}\varepsilon_{\mathrm{eq}}.$$

In order to determine TF_{avg} one must know the failure strain appearing in (12): if ε_f is already known, there is no need for using any damage model. So for using the W1 model as a predictive tool, it can be put in a different form:

$$(13) \qquad D(\varepsilon_{\mathrm{eq}}) = \int_0^{\varepsilon_{\mathrm{eq}}} TF(\varepsilon_{\mathrm{eq}}) \cdot \mathrm{d}\varepsilon_{\mathrm{eq}} \leq D_{\mathrm{cr}}.$$

Local failure occurs when $D(\varepsilon_{\mathrm{eq}})$ reaches the critical value D_{cr}, which is a material constant. Then, as for the Tresca model, W1 failure predictions are carried out by simulating the load history of a structure by finite elements and seeking when and where the critical condition is met firstly.

A successive model by Wierzbicki, identified as the W2 model, presented in [5] and slightly modified in [9], is based on the following equation:

$$(14) \qquad \varepsilon_f = D_1(\vartheta_N) \cdot e^{D_2(\vartheta_N) \cdot TF_{\mathrm{avg}}} = D_1(\vartheta_N) \cdot e^{D_2(\vartheta_N) \cdot \cdot \frac{1}{\varepsilon_f} \int_0^{\varepsilon_{\mathrm{eq}\,f}} TF(\varepsilon_{\mathrm{eq}}) \cdot \mathrm{d}\varepsilon_{\mathrm{eq}}}.$$

The effect of TF is included in the exponential relationship, while the effect of the Lode angle is given by the two functions $D_1(\theta_N)$ and $D_2(\theta_N)$, characteristic of each material.

A damage function can be derived from (14), expressing the ratio of the current local strain to the right-hand term of (15):

$$(15) \qquad D(\varepsilon_{\mathrm{eq}}) = \frac{\varepsilon_{\mathrm{eq}}}{D_1(\vartheta_N) \cdot e^{D_2(\vartheta_N) \cdot \cdot \frac{1}{\varepsilon} \int_0^{\varepsilon_{\mathrm{eq}}} TF(\varepsilon_{\mathrm{eq}}) \cdot \mathrm{d}\varepsilon_{\mathrm{eq}}}} \leq 1,$$

$$D(\varepsilon_f) = D_{\mathrm{cr}} = 1.$$

It is a purely conventional damage function representing the ratio between the current strain and the failure strain for a given TF history, in fact the critical value of D is material independent.

In model W1 the dependence on θ_N is not included and the three-dimensional surface $\varepsilon_f(TF_{\mathrm{avg}}, \theta_N)$ degenerates into a curve $\varepsilon_f(TF_{\mathrm{avg}})$, while, according to the W2 model, the surface of failure strains may be transformed in a set of curves $\varepsilon_f(TF_{\mathrm{avg}})$, each parametrized with respect to θ_N and having two constants substituting the functions $D1$ and $D2$.

In fig. 4 are reported two typical curves expressing the failure criteria W1 with $D_{\mathrm{cr}} = 0.15$ for whatever Lode angle, and the criteria W2 with $D1 = 0.4534$ and $D2 = -0.7788$ for $\theta_N = 1$. These data refer to a 2420 T351 aluminium alloy and are available in [32] and [9] provided that failure is symmetric with respect to tension and compression.

According to fig. 4, a strain history DC at constant triaxiality up to failure, induces the same failure condition of a strain path AB at a constant triaxiality lower than before, followed by a successive loading path BC at a triaxiality great enough that further
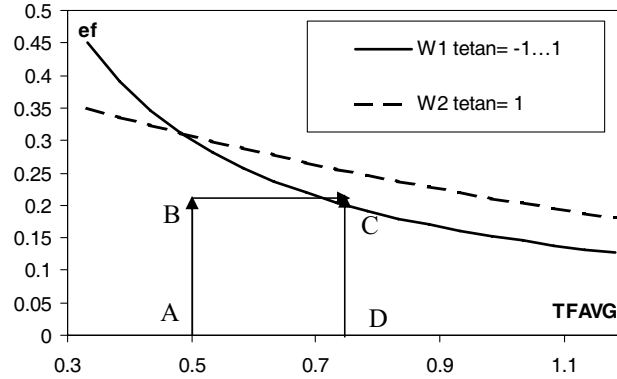
Fig. 4. – Fracture loci curves as a function of TFAVG.

plastic strain before failure is prevented. This corresponds to say that ductile damage is independent of the strain-triaxiality path, which is not possible for highly dissipative phenomena like ductile failure.

Then, curves like those in fig. 4 may help in failure predictions only if both triaxiality and Lode angle are held constant during a load history so that their average values coincide with initial values, but this is a special case of proportional loading and is quite a rare occurrence in plastic straining. For the large majority of real strain histories, TF and θ_N are subjected to significant variations as plastic strains locally flows and the shape of the loaded structures is distorted, so the damage models like W1 and W2 have to be used in the form of conditional inequalities as in eqs. (13) and (15) rather than being used as limit curves or failure criteria.

In the next sections of the paper the above procedure is to be applied to the W1 model and to the finite elements analyses simulating experimental tests up to complete failure. Instead the W2 and Tresca models are used only for predicting failure initiation at a material point rather than the complete breaking of specimens.

3. – Finite elements and failure prediction

Finite elements (FE) simulations of the experimental tests are performed with the commercial code MSC-MARC. Four-noded axisimmetric elements are used for modeling the round specimens, while, for the notched plates, 8-noded tetrahedral elements are used; displacements are imposed at the prescribed nodes for simulating the motion of the test machine crosshead or loading pins. All the analyses are based on the updated Lagrangian formulation for large displacements and finite strains, and the additive plasticity procedure is based on the von Mises yield criterion with isotropic hardening only.

The curves $\sigma_{eq}(\varepsilon_{eq})$ in fig. 3 are used for defining the stress-strain behavior of the various metals in the FE simulations. A preliminary assessment of the accuracy of the FE analyses and damage models is made from a macroscopic point of view by comparing experimental and numerical true stress-true strain curves or load-displacement curves, and true strain at failure ε_F.

The true strain ε_F is the mean value of the current distribution of ε_{eq} above the neck section at the instant when failure initiaties at a single element; instead ε_f is the peak local value of the same strain distribution at the same instant of each test.
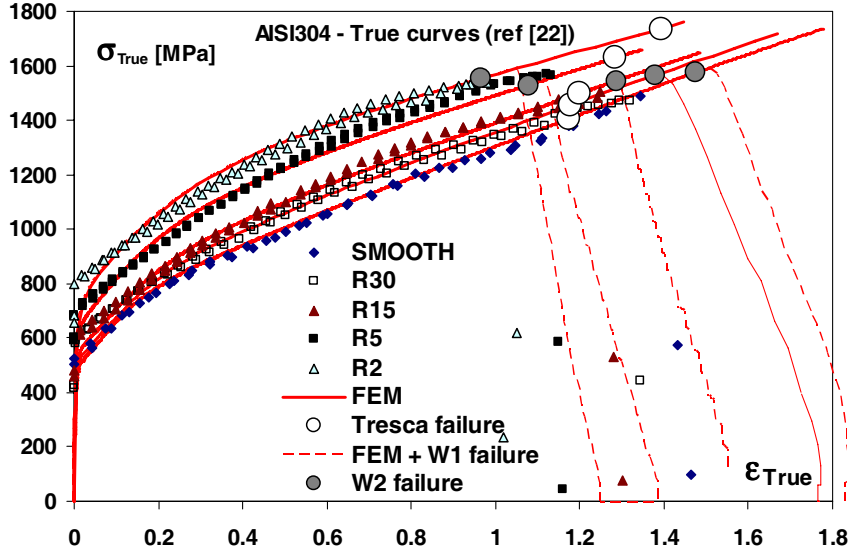
Fig. 5. – True stress-true strain curves for AISI304 with failure estimations.

Then a second assessment of the accuracy of failure models is made by comparing the local values of ε_f and TF from the various damage models with the same values calculated from the analyses stopped at the analysis step corresponding to experimental failure.

Results for each material are presented separately and a common discussion for the whole set of experiments will made in the conclusions.

3˙1. *AISI 304.* – The prediction of failure for the AISI304 steel is made by assuming for each specimen that the critical true strain ε_F is that of the last point at the end of the descending branch of the experimental true curves, as it was made in [34] for this metal. The following parameters are then obtained: $D_{cr} = 1$, $D1 = 3.8$, $D2 = -1.4$, $\tau_{cr} = 588\,\mathrm{MPa}$, and the corresponding results are shown in figs. 5 and 6.

While the agreement between the two Wierzbicki models and experimental data is good in terms of the local variables of fig. 6, a certain overestimation of the true strain at failure initiation is found in fig. 5, where the W1 and W2 predictions for ε_F are closer to complete failure than to failure initiation. This occurs because the experimental values of ε_F used for determining the material constants correspond to the fracture almost completely propagated through the resisting section rather than corresponding to the peak of true stress which indicates fracture initiation.

Due to the low number of experimental points available in the final stages of the tensile tests, the real true stress peak and the real failure initiation are determined with a certain approximation, in fact failure may occur at whatever strain within the strain interval extending for about 0.05 or 0.1 between the recorded peaks of true stress and the final points of the true curves.

Frequently, the descending branch of an experimental true curve is either not detectable or is only roughly described by very few stress-strain points due to the rapidity of the crack propagation process. Approximations may arise in the latter cases, due to possible ambiguities in the choice of the data for calibrating the damage models.
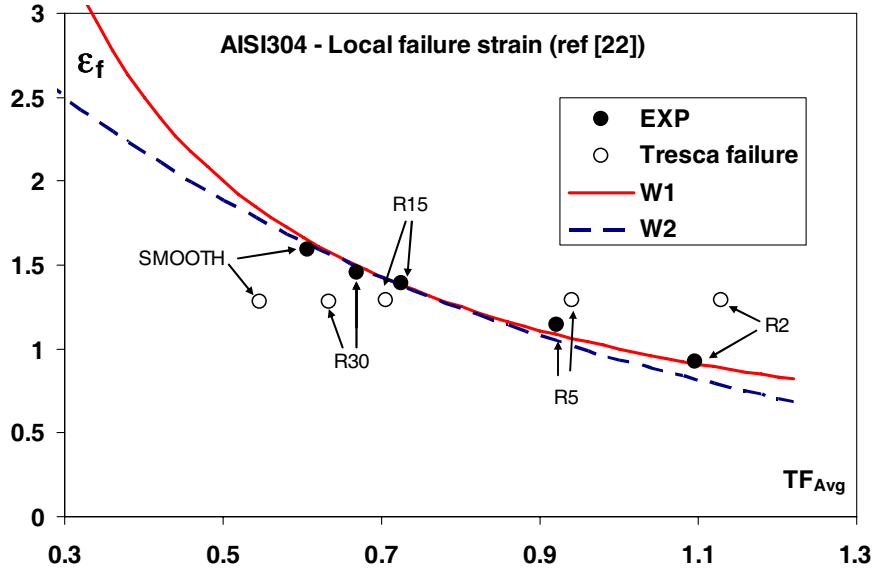
Fig. 6. – Local failure strain for AISI304 as a function of local average triaxiality.

The notches tested for this metal are not sharp enough, so failure initiates always at the neck center and the local-scale parameters follow the usual trend: TF_{avg} increases and ε_f decreases as the notch severity increases, while the angle θ_N remains equal to 1 during the entire test due to axisymmetry of stress and has no influence on the whole failure initiation.

3˙2. FE370. – For this metal the experimental failure strains ε_F are determined as the peak points of each stress strain curve before the descending branch of the curve, and the corresponding material parameters for damage are $D_{\mathrm{cr}} = 0.64$, $D1 = 2.5$, $D2 = -1.4$, $\tau_{\mathrm{cr}} = 341\,\mathrm{MPa}$.

For this metal, the results for the round specimens are shown in fig. 7 while those for the notched plates are reported in fig. 8, where only the numerical curves simulating the W1 damage evolution are presented.

The simulated true stress-true strain data from round tensile bars are quite close to experimental data and a maximum discrepancy of 5% is found between the average experimental data and the numerical data. Quite larger is the numerical error found in the load displacement curves for the notched plates, in fact the simulated curve for R2 plates underestimates the load of more than 15%.

Instead, the failure prediction in terms of local strain ε_f of fig. 9 is quite accurate for both round specimens and flat plates. To investigate about this aspect, the damage-related parameters, TF and θ_N, are calculated at the material points where failure initiates. According to the FE simulations and, for the round specimens, to the experimental confirmation given by the cup-cone shape of the fracture surface, failure starts at the neck center for the round specimens and just below the external surface in the area of the notch root for the notched plates, as visible in fig. 10.

As visible in fig. 11, the triaxiality varies during the entire straining history by increasing at the center of necking of round bars and by decreasing at the failure initiation
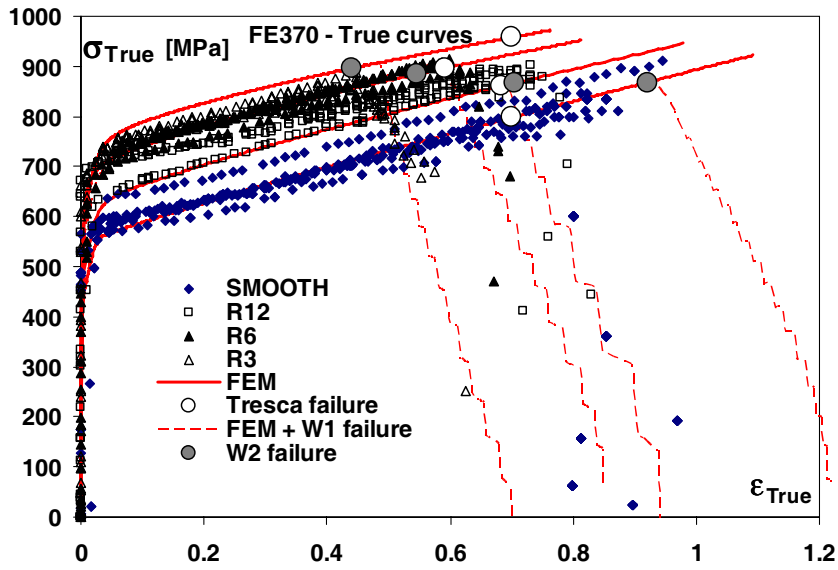
Fig. 7. – True stress-true strain curves for FE370 with failure estimations.
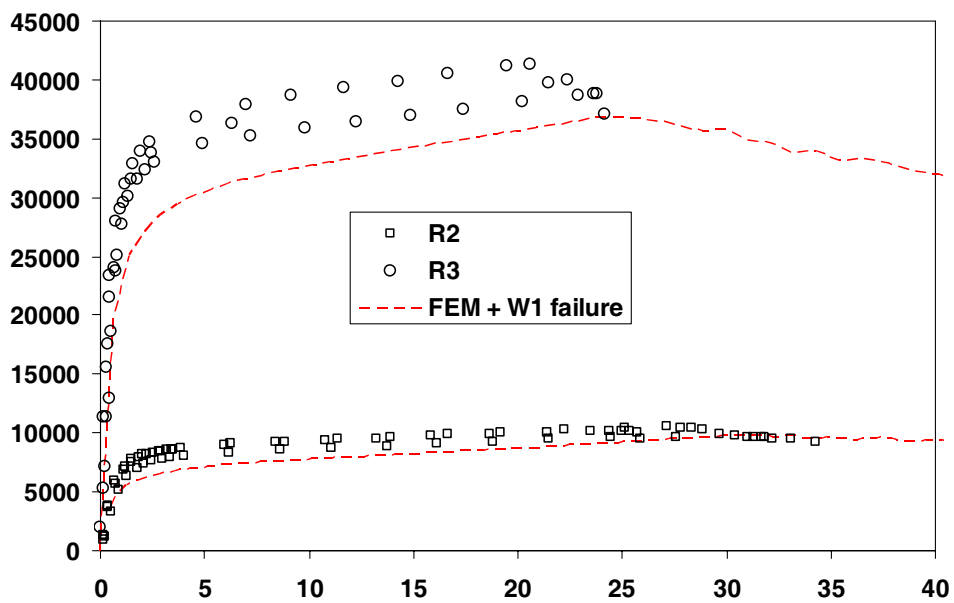
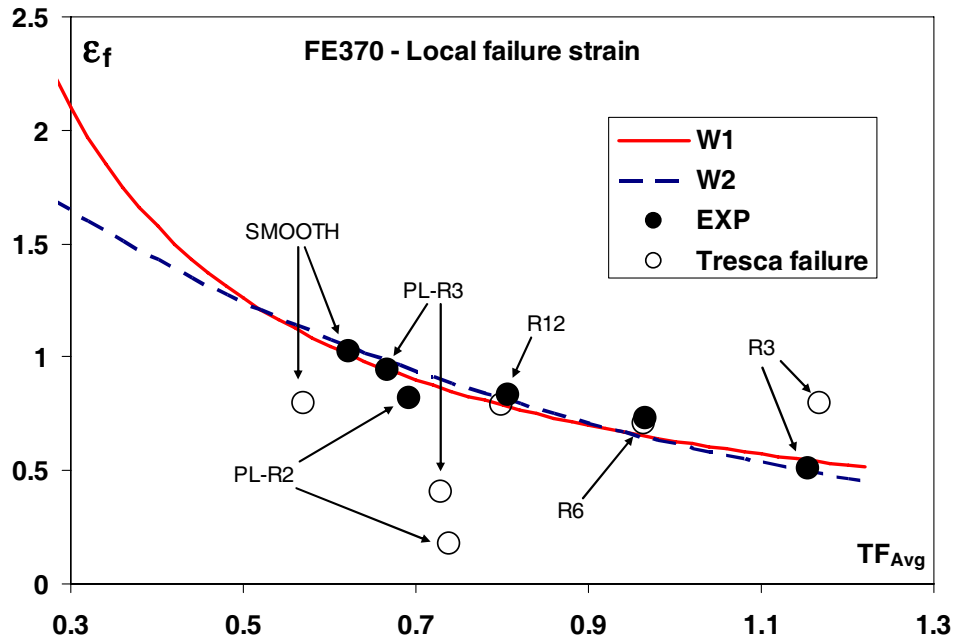Fig. 8. – Load *vs.* notch opening curves for the notched plates of FE370.

Fig. 9. – Local failure strain for FE370 as a function of local average triaxiality.

site of notched bars, but the overall range of TF variability is the same for both bars and plates. On the contrary, the θ_N angle evolves in definitely different ways in fact, at the neck center of bars it is always $= 1$ because of the axisimmetry of the stress state, while at failure sites of plates it is again constant but its value is lower (for plate R3) and much lower (plate R2) than it is for bars. Further investigation is useful for confirming the results presented but, according to this set of experiments and simulations, it seems that the Lode angle influences strongly the stress-strain characterization (see fig. 7) but does not play a great role on the failure phenomena, as indicates in fig. 8 where failure curves W1 and W2 simulate in a resonable way all failure points from round bars as well as the points from.
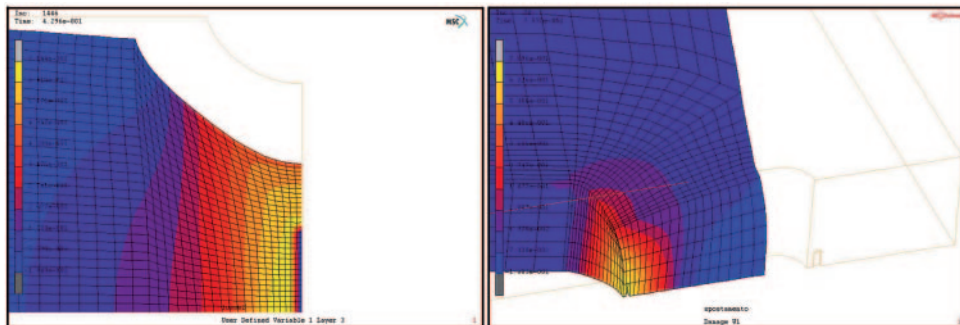

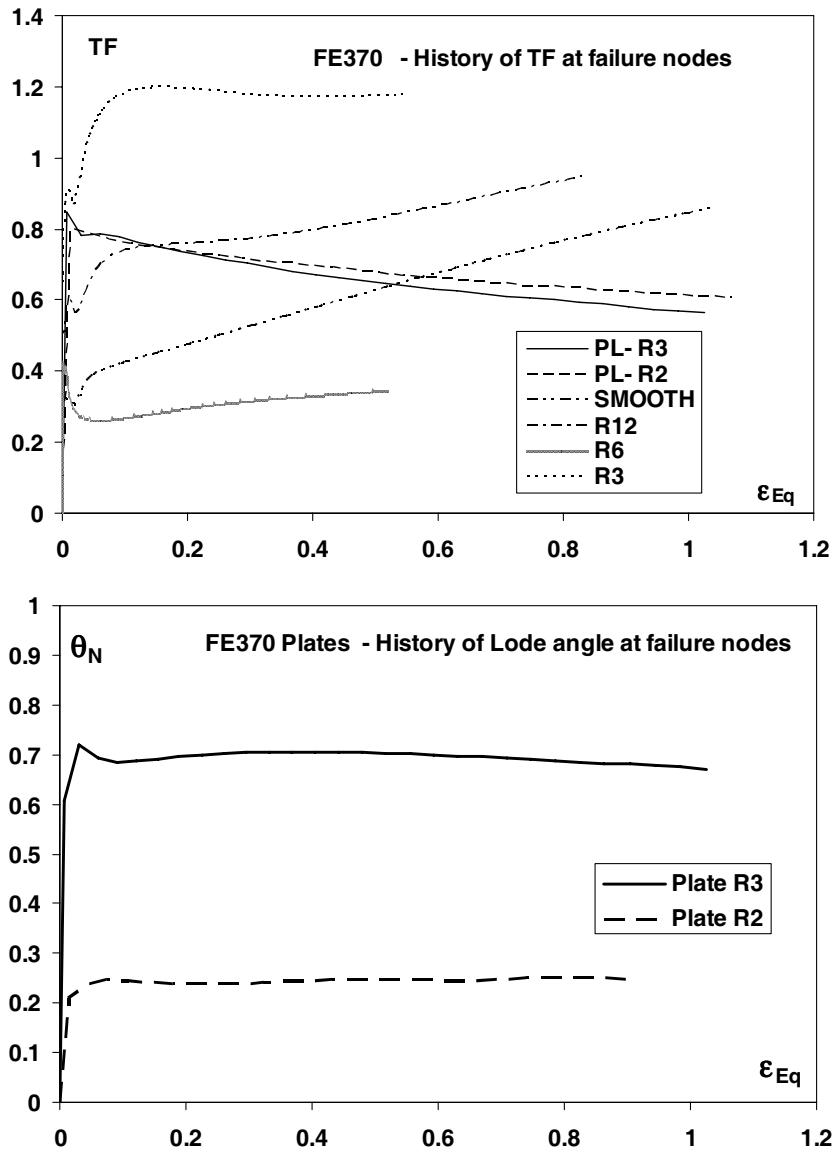Fig. 10. – Fracture initiation and distribution of W1 damage.

Fig. 11. – Triaxiality and Lode angle for FE370 as a function of local equivalent plastic strain.

4. – Conclusions

The modelling of ductile damage according to different theories is performed in this paper with reference to round bars with and without notch, other than to flat plate notched specimens.

For characterizing the stress-strain behaviour of elastoplastic metals at large strains the approximate MLR method is adopted, consisting of a corrective function for the true stress which applies to various ferrous, aluminium-based and copper-based ductile alloys undergoing monotonic loading at very low strain rates.

Finite-elements simulations are run without any damage model and with a subroutine able to eliminate elements when the W1 critical damage is reached. The results of FE simulations in terms of stress-strain data are poorly accurate for notched plates while they are satisfactory for the reproduction of round specimens. Instead the damage prediction, in terms of local failure strain and local history-averaged TF, is satisfactory for all the specimens tested.

The logarithmic strains at failure are slightly less accurate than local values are, and both W1 and W2 models exhibit very similar predictions in the range of triaxialities and Lode angle values investigated.

The known effect of stress triaxiality on reducing local failure strains is confirmed, but the expected role of the Lode angle which should reduce the failure strain as plane strain approaches, is not found by the data above.

In theory fracture propagation can be easily simulated by FE but the mesh-dependence issues coupled to the need of gradually deleting elements deserves more efforts to determine the right mesh size for every model.

The overall accuracy of both Wierzbicki models is satisfactory in the range of triaxiality and Lode angle investigated in this paper.

REFERENCES

[1] McClintock F. A., *J. Appl. Mech.*, **35** (1968) 363.
[2] Rice J. R. and Tracey D. M., *J. Mech. Phys. Solids*, **17** (1969) 201.
[3] Mackenzie A. C., Hancock J. W. and Brown D. K., *Eng. Fract. Mech.*, **9** (1977) 167.
[4] Hancock J. W. and Mackenzie A. C., *J. Mech. Phys. Solids*, **24** (1976) 147.
[5] Wierzbicki T., Bao Y., Lee Y.-W. and Bai Y., *Int. J. Mech. Sci.*, **47** (2005) 719.
[6] Wierzbicki T., *Fracture of AHSS sheets and status of the AHSS Consortium at MIT*, posted on the website of Impact Crashworthiness Laboratory: `http://web.mit.edu.icl`.
[7] Barsoum I. and Faleksog J., *Int. J. Solids Struct.*, **44** (2007) 1768.
[8] Bigoni D. and Piccolroaz A., *Int. J. Solids Struct.*, **41** (2004) 2855.
[9] Bai Y. and Wierzbicki T., *Int. J. Plast.*, **24** (2007) 1071.
[10] Mirone G., *Int. J. Solids Struct.*, **41** (2004) 3545.
[11] Mirone G., *Mech. Mater.*, **40** (2008) 685.
[12] Bridgman P. W., *Studies in Large Flow and Fracture* (McGraw Hill) 1956.
[13] Zhang Z. L., Hauge M., Odegard J. and Thaulow C., *Int. J. Solids Struct.*, **36** (1999) 2386.
[14] Alexandrov S. E. and Goldstein R. V., *Int. J. Fract.*, **91** (1998) 1.
[15] Alves M. and Jones N., *J. Mech. Phys. Solids*, **47** (1999) 643.
[16] La Rosa G., Mirone G. and Risitano A., *Metall. Mater. Trans. A*, **34** (2003) 615.
[17] Lemaitre J., *J. Eng. Mater. Technol.*, **107** (1985) 83.
[18] Chaboche J. L., *J. Appl. Mech.*, **55** (1988) 59.
[19] Bonora N., *Eng. Fract. Mech.*, **58** (1997) 11.
[20] Wang T. J., *Eng. Fract. Mech.*, **42** (1992) 177.
[21] La Rosa G., Mirone G. and Risitano A., *Eng. Fract. Mech.*, **68** (2001) 417.
[22] Gurson A. L., *AMSE Trans., J. Eng. Mater. Technol.*, **99** (1977) 2.
[23] Tvergaard V. and Needleman A., *Acta Metall.*, **32** (1984) 157.
[24] Pardoen T., Doghri I. and Delannay F., *Acta Mater.*, **46** (1998) 541.
[25] Ragab A. R., *Eng. Fract. Mech.*, **71** (2004) 1515.
[26] Gologanu M., Leblond J.-B., Perrin G. and Devaux J., *Recent extensions of Gurson's model for porous ductile metals*, in *Continuum Micromechanics* (Springer-Verlag) 1997; Chapt. 2, pp. 61-130.
[27] Le Roy G., Embury J. D., Edwards G. and Ashby M. F., *Acta Metall.*, **29** (1981) 1509.

[28] Mirone G., *Int. J. Damage Mech.*, **13** (2004) 241.
[29] Schiffmann R., Heyer J. and Dahl W., *Eng. Fract. Mech.*, **70** (2003) 1543.
[30] Chaouadi R., De Meester P. and Vandermeulen W., *Int. J. Fract.*, **66** (1994) 155.
[31] Johnson G. R. and Cook W. H., *Eng. Fract. Mech.*, **21** (1985) 31.
[32] Bao Y. and Wierzbicki T., *Int. J. Mech. Sci.*, **46** (2004) 81.
[33] Bao Y. and Wierzbicki T., *ASME J. Eng. Mater. Technol.*, **126** (2004) 314.
[34] Mirone G., *Eng. Fract. Mech.*, **74** (2007) 1203.